Defect Detection in Solar Modules Using ICA Basis Images

Du-Ming Tsai, *Member, IEEE*, Shih-Chieh Wu, and Wei-Yao Chiu

Abstract—Solar power has become an attractive alternative of electricity energy. Solar cells that form the basis of a solar power system are mainly based on multicrystalline silicon. A set of solar cells are assembled and interconnected into a large solar module to offer a large amount of electricity power for commercial applications. Many defects in a solar module cannot be visually observed with the conventional CCD imaging system. This paper aims at defect inspection of solar modules in electroluminescence (EL) images. The solar module charged with electrical current will emit infrared light whose intensity will be darker for intrinsic crystal grain boundaries and extrinsic defects including micro-cracks, breaks and finger interruptions. The EL image can distinctly highlight the invisible defects but also create a random inhomogeneous background, which makes the inspection task extremely difficult.

The proposed method is based on independent component analysis (ICA), and involves a learning and a detection stage. The large solar module image is first divided into small solar cell subimages. In the training stage, a set of defect-free solar cell subimages are used to find a set of independent basis images using ICA. In the inspection stage, each solar cell subimage under inspection is reconstructed as a linear combination of the learned basis images. The coefficients of the linear combination are used as the feature vector for classification. Also, the reconstruction error between the test image and its reconstructed image from the ICA basis images is also evaluated for detecting the presence of defects. Experimental results have shown that the image reconstruction with basis images distinctly outperforms the ICA feature extraction approach. It can achieve a mean recognition rate of 93.4% for a set of 80 test samples.

Index Terms—Defect detection, independent component analysis, surface inspection, solar module.

I. INTRODUCTION

SOLAR power has become an attractive alternative of electricity energy due to growing environmental concerns and global oil shortage. Solar cells that convert the photons from the sun to electricity are mostly based on crystalline silicon in the current market because it can generate good performance in usable lifespan and conversion efficiency among the currently available techniques. Multicrystalline solar cells are more popular than monocrystalline solar cells. They dominate the production volume in the photovoltaic industry due to lower manufacturing costs.

The surface of a multicrystalline solar wafer shows multiple crystal grains of random shapes and sizes in random positions
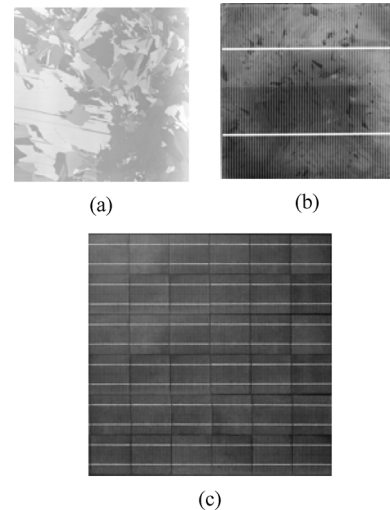
Fig. 1.   CCD-captured images of (a) multicrystalline solar wafer; (b) solar cell; (c) solar module composed of 36 solar cells.

and orientations. It results in a heterogeneous texture in the surface. No two solar wafer surfaces contain completely identical patterns. A solar wafer is a thin slice of a silicon ingot. It is further processed and fabricated into a solar cell that forms the basic unit of a solar power system. A set of solar cells are assembled and interconnected into a solar module to offer a large amount of electricity power for a variety of commercial applications.

Fig. 1(a) shows the image of a defect-free multicrystalline solar wafer. It contains random crystal grains on the surface. Fig. 1(b) is a solar cell image taken by a typical charge-coupled-device (CCD) camera, where the vertical thin metal strips are finger electrodes that supply current to the two horizontal thick bus bars. The bus bars are used for interconnecting solar cells to make a solar module. Fig. 1(c) demonstrates a CCD-captured solar module image. It is composed of a matrix of 36 (6×6) solar cells.

Image processing techniques have become an important tool for biometric recognition [1], [2], robotic automation [3], [4] and industrial inspection [5]–[7]. The quality inspection of a solar module in manufacturing is very important to ensure the expected conversion efficiency and durable lifespan. A few automatic defect detection algorithms in the literature have been focused on the detection of defects in solar wafers and solar cells. The inspection in the early manufacturing stages can prevent delivering defective materials to the subsequent process. However, some of critical defects including micro-cracks, breaks and finger interruptions may inevitably occur in solar modules during the transportation, handling and

assembly. Fuyuki and Kitiyanan [8] have also pointed out that the point-pressure cracks due to the failure in the metal wire soldering could occur in the solar module assembly process. The defects of a solar module may reduce the current or even consume the power stored in the battery bank. They may also cause thermal effect that deteriorates the materials and eventually shorten the lifespan of the solar module. This paper proposes an efficient machine vision scheme for automatic defect detection in multicrystalline solar modules. It can detect subtle defects in solar modules with inhomogeneous surfaces, and is computationally very fast to implement. It requires no complicated feature design and feature extraction process for distinguishing local defects from a wide variety of crystal grain patterns.

Due to the random crystal grain surface of a solar cell or interior defects that do not visually appear on the cell surface, automatic defect detection in solar modules with the typical CCD camera and lighting system cannot be effectively realized. In order to highlight the deficiencies that degrade the conversion efficiency of a solar module, the electroluminescence (EL) imaging technique [8]–[10] has been proposed in recent years. In the EL imaging system, current is sent through a solar module in a darkened room, and then a cooled Si-CCD or InGaAs camera is used to capture the infrared light emitting from the excited solar module. Areas of crystal silicon with higher conversion efficiency exhibit brighter luminescence in the sensed image. Process deficiencies such as micro-cracks, breaks and finger interruptions will appear as dark regions because they are inactive and hardly emit light. The dislocation and grain boundary of silicon wafers also create dark regions in the background of the EL image. Because the crystal grain pattern is random and unique for each individual multicrystalline solar wafer, the crystal grain backgrounds of all solar cells in a solar module are also randomly present in the EL image. This causes automatic defect detection of solar modules in EL images extremely difficult.

Fig. 2(a) and (b) demonstrates the EL images of a defect-free and a defective solar module, respectively. As seen in Figs. 1(c) and 2(b), the solar module captured in the CCD image cannot detect the inner micro-cracks and some subtle local defects, while the EL image can well present various defects embedded in the solar module. Fig. 3(a)–(c) further shows three enlarged solar cell subimages in a solar module, which contain respectively micro-crack, break and finger interruption. As seen in Fig. 2(a), each solar cell in the solar module presents a random background pattern. The defective solar cells in a solar module can be visually present in the EL image, as shown in Fig. 2(b).

Because a typical solar module is composed of multiple solar cells in series, the image size of a solar module is generally very large. However, the local defects of a small solar cell in the module image could be very small. The large image size with a low resolution of defects demands a very efficient and yet very effective automatic visual inspection scheme for defect detection of multicrystalline solar modules in EL images.

As aforementioned, most of the machine vision algorithms for defect detection in the photovoltaic industry are mainly focused on the process levels of solar wafers and solar cells. Fu *et al.* [11] presented a machine vision method to detect cracks
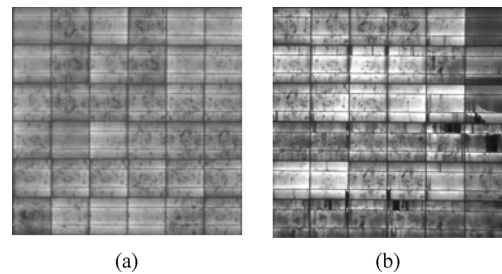

Fig. 2. Demonstrative EL images of (a) defect-free solar module, and (b) defective solar module.
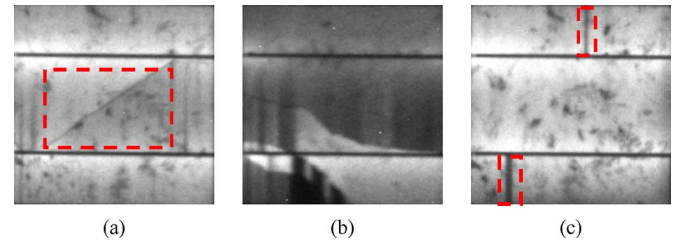

Fig. 3. Defect types of solar cells displayed in the EL image: (a) micro-crack; (b) break; (c) finger interruption.

in solar cells by evaluating the geometric features of the defect. The method can only identify cracks occurred in the cell edges with distinct gray levels from their surrounding. Ordaz and Lush [12] analyzed the conversion efficiency of a solar cell based on the gray-level distribution in the EL image. The gray-level histogram gives only the information about the overall proportion of dark regions in the EL image. It cannot be used to detect the presence/absence of local small defects in the EL image. Pilla *et al.* [13] used the thermographic technique to highlight cracks in solar cells.

Recently, Tsai *et al.* [14] presented an anisotropic diffusion algorithm for detecting micro-cracks appeared on the solar wafer surface. The sensed image is obtained from a typical CCD camera and light source that shows the cracks with low gray levels and high gradients. The diffusion process smoothes the suspected defect region and preserves the crystal grain background. The crack location can then be well detected by subtracting the diffused image from the original image. The method is specifically designed to identify micro-cracks by assuming micro-cracks present darker intensity and higher gradient from their surrounding in the CCD-captured image. The typical CCD image cannot detect the invisible inner cracks and the algorithms can only detect the specific outer micro-cracks in solar wafers. Tsai and Luo [15] further proposed a mean-shift algorithm to detect three defect types of saw-mark, fingerprint and contamination in multicrystalline solar wafers. The target defects generally present high variation of gradient directions, while crystal grain edges show more consistent gradient directions. The original gray-level wafer image is first converted into an entropy image, where each pixel defined in a small neighborhood window is represented by the entropy of gradient directions. The mean-shit smoothing process is then performed to remove noise and grain edges in the entropy image. The final edge points remained in the filtered image are identified as defective ones. Chiou *et al.* [16] used a near infrared imaging

system to detect micro-cracks in solar wafers. The intensities of a micro-crack are darker than those of the surrounding grain background in the sensed image. A local thresholding and a region-growing segmentation, followed by morphological post-processing and blob analysis, are used to detect the dark micro-cracks. The method is performed in the solar wafer process, but not in the final solar module process. It is assumed that the sensed micro-crack is significantly darker than the crystal grains by infrared lighting. A dark, thin elongated crystal grain in the defect-free solar wafer could be falsely detected as a defect. It cannot be directly extended for detecting various defect types found in solar modules.

The currently available defect detection algorithms reviewed above are generally applied to detect defects with distinct geometric and intensity features, or are computationally intensive to detect defects in a high-resolution image. Since the EL image of a solar module under inspection is generally very large in size and local defects in a solar cell subimage is relatively very small in a random background, we need a fast detection algorithm to screen all possible defective solar cells in the large solar module image.

The proposed method is based on the independent component analysis (ICA) technique [17]. ICA is a novel statistical signal processing technique to extract independent sources given only observed data that are mixtures of unknown sources without any prior knowledge of the mixing mechanism. It has been applied in texture analysis [18], [19] that uses either the estimated independent components or the column vectors of the estimated mixing matrix as features for texture classification/segmentation. The ICA techniques have also been applied for surface defect detection of textile fabrics [20], [21] and liquid crystal display (LCD) panels [22] in manufacturing, and for grading tomato ripening [23] in agriculture. All the ICA-based defect detection methods are only applicable to non-textured or homogeneously-textured surfaces. They cannot be extended for defect detection in the EL images with inhomogeneous background patterns.

The proposed ICA-based defect detection scheme involves a learning process and an inspection process. Each solar module image is first partitioned into individual solar cell subimages. In the learning process, a set of defect-free solar cell subimages are randomly chosen from different solar modules. Each 2D solar cell subimage used for training is reshaped as a 1D signal and forms a row vector in the data matrix. The ICA technique is then used to find a set of statistically independent basis images from the training data matrix. In the inspection process, the solar module image is also first divided into individual solar cell subimages. A test solar cell subimage is reconstructed as a linear combination of the learned basis images. It is expected that a defect-free solar cell subimage can be well represented by the basis images and the reconstructed image of a defective solar cell subimage will be distinctly deviated from its original one.

In this study, we evaluate two ICA-based approaches for identifying the presence or absence of defects in a solar cell subimage. The first approach is based on feature extraction and the second approach is based on image reconstruction from ICA basis images. The first ICA approach uses the coefficients of the linear combination of basis images as the feature vector. It is then compared with that of each training sample in the data set by a distance measure, and the minimum distance among all training samples is used as the discrimination measure. The second ICA approach simply calculates the reconstruction error between the original solar cell subimage under inspection and its reconstructed image from the basis images. If the distance or reconstruction error is larger than a predetermined threshold, it is identified as a defective solar cell subimage. Otherwise, it is declared as a defect-free subimage. The performance between these two ICA-based approaches will be evaluated by a set of EL images of solar modules. The proposed method can fast detect the presence/absence of defects in solar modules, but it cannot identify the actual shape and location of a defect in the image.

The paper is organized as follows: Section II first discusses the basic ICA model, followed by the process for extracting independent basis images from a set of training samples. The feature extraction and image reconstruction from the ICA basis images for detecting the presence/absence of defects in an inspection image are then presented. Section III evaluates the performance of the proposed ICA-based detection methods and analyzes the effect of changes in the number of basis images. The comparative study between the proposed method and the existing methods of adaptive thresholding and gray-level morphology is also presented in this section. The paper is concluded in Section IV.

II. ICA BASIS IMAGES FOR DEFECT DETECTION

The EL image of a multicrystalline solar module investigated in this study present multiple solar cell subimages, each containing randomly-shaped dark regions in the background. The critical defects found in a solar module are micro-cracks, breaks and finger interruptions. They are present as dark line- or bar-shaped regions, or divide a region into a bright and a dark area in the EL image, as seen in Fig. 3(a)–(c). There are no straightforward features based on geometric shapes and intensities to distinguish the difference between defect regions and the dark regions in the background. The proposed method uses ICA to find a set of representative basis images that can best describe various defect-free solar cell subimages. Each solar cell subimage partitioned from a large EL image of solar module is then represented as a linear combination of the basis images.

In order to inspect individual solar cells in the large solar module, the solar cells in the whole EL image must be partitioned into small subimages, each containing exactly one solar cell. It can be observed from the solar module image in Fig. 2 that the spacing between adjacent solar cells in either horizontal or vertical direction is straightly and continuously dark in the whole EL image of a solar module. Horizontal and vertical projections that accumulate the gray levels of each row and column in the solar module image are first constructed. The local valleys (i.e., local minima) of the projection then indicate the spacing between adjacent solar cells. Two adjacent local valleys in the same projection direction are fine-tuned so that each partitioned solar cell subimage gives the same size.
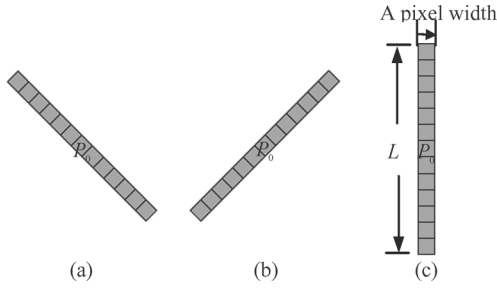
Fig. 4. Three line structuring elements in directions (a) 135°, (b) 45° and (c) 90° for background smoothing.

The proposed defect detection scheme in this paper includes the off-line learning of ICA basis images and the on-line detection of defective subimages. For either off-line learning or on-line detection, a solar module must be first partitioned into solar cell subimages using the gray-level projection described above. The subsequent learning and detection processes are all carried out for solar cell subimages. In the off-line learning stage, the ICA model is used to find a set of independent basis images from randomly sampled defect-free solar cell subimages. In the on-line detection stage, feature extraction and image reconstruction from the basis images are used to evaluate the presence/absence of defects in the inspection image. In the following subsections, a morphological preprocessing for image smoothing is first present. The basis ICA model is then briefly discussed, followed by the off-line learning of independent basis images. The on-line detections with feature extraction and image reconstruction are finally described.

A. Morphological Smoothing

As seen in Fig. 2, each solar cell subimage presents a random dark-region pattern in the background. Some of the dark regions are similar to the defect regions. In order to smooth the dark-region background and preserve the defect shapes in the EL image, a specific morphological smoothing process is preformed first in the EL image before it is used for off-line learning and on-line detection. As observed in Fig. 3(a)–(c), defects of micro-cracks, breaks and finger interruptions are mostly line- or bar-shaped. We therefore design three structuring elements (SEs) in the directions of 45°, 90° and 135°, each of length L pixels and width 1 pixel, as shown in Fig. 4.

The length L is generally larger than the largest dimension of a random dark region but smaller than the defect length so that most of the dark regions in the background can be smoothed, and yet the defects can be well preserved in the filtered image. In this study, the length L is given by 13. For a given pixel point (x, y) with gray level $f(x, y)$, the gray levels in each of the three SEs are accumulated. Given the origin of the image in the upper-left corner, we have

$$S_{135}(x, y) = \sum_{i=-L/2}^{L/2} f(x+i, y+i) \quad \text{for } 135°-\text{SE}$$

$$S_{45}(x, y) = \sum_{i=-L/2}^{L/2} f(x-i, y+i) \quad \text{for } 45°-\text{SE}$$

$$S_{90}(x, y) = \sum_{i=-L/2}^{L/2} f(x, y+i) \quad \text{for } 90°-\text{SE}.$$

It is expected that a line- or bar-shaped defect will have a very small accumulated magnitude. We thus select the SE with the minimum accumulated gray levels. Let θ-SE be the corresponding structuring element with a minimum accumulated magnitude among the three directions, i.e.,

$$\theta-\text{SE} = \arg\min\{S_{45}(x, y), S_{90}(x, y), S_{135}(x, y)\}.$$

Once the structuring element θ-SE is chosen, the gray-level dilation (i.e., local maximum gray level) is applied to the solar cell subimage with the structuring element in direction θ. That is

$$f(x, y) = \max\{f(x+i, y+j), \forall(x+i, y+j) \in \theta-\text{SE}\}.$$

If θ-SE contains all defect points, the dilated value will be still small for a dark region. Otherwise, the dilated value will be large for a bright region in the background. In this study, we do not use a horizontal structuring element (i.e., 0°-SE) because we would like to remove the two horizontal thick bus bars in the solar cell subimage. Fig. 5(a1)–(d1) shows, respectively, a defect-free and three defective solar cell subimages in the EL images. Fig. 5(a2)–(d2) presents the corresponding morphological smoothing results of Fig. 5(a1)–(d1). The filtering results show that the dark regions in the background are better smoothed while all the defects of micro-crack, break and finger interruption are well preserved. The morphological smoothing process allows a better extraction of representative basis images in the ICA learning stage and a better image reconstruction in the detection stage.

B. ICA Model and Basis Images

In the ICA model [17], [24], the observed mixture signals $\mathbf{X}$ can be expressed as

$$\mathbf{X} = \mathbf{A} \cdot \mathbf{S} \tag{1}$$

where $\mathbf{A}$ is an unknown mixing matrix; $\mathbf{S}$ represents the latent source signals, meaning that they cannot be directly observed from the mixture signals $\mathbf{X}$. The ICA model describes how the observed mixture signals $\mathbf{X}$ are generated by a process that uses the matrix $\mathbf{A}$ to mix the latent source signals $\mathbf{S}$. The source signals are assumed to be mutually statistically independent. Based on this assumption, the ICA solution is obtained by finding a demixing matrix $\mathbf{W}$. It is used to linearly transform the observed mixture signals $\mathbf{X}$ to yield the estimated independent signals $\mathbf{U}$ with

$$\mathbf{U} = \mathbf{W} \cdot \mathbf{X}. \tag{2}$$

The separated components in $\mathbf{U}$, called independent components (ICs), are required to be as mutually independent as possible. The matrix $\mathbf{U}$ is an estimate of the latent source signals $\mathbf{S}$.

There exist many algorithms performing ICA [25]–[29]. FastICA [26], [30] is one of the most widely used techniques to solve for the ICA model due to its computational efficiency and effectiveness for source separation. The objective of an
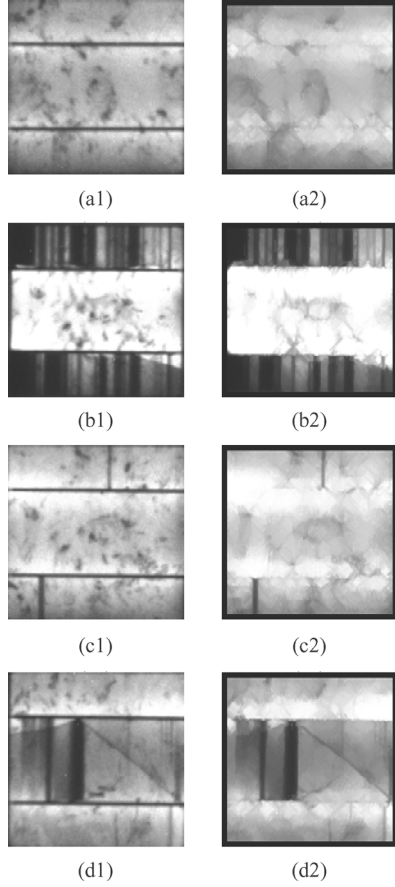
Fig. 5. Morphological smoothing on solar cell subimages: (a1) defect-free sample; (b1)–(d1) three defective samples; (a2)–(d2) respective smoothing results of (a1)–(d1).

ICA model is to maximize the statistical independency of ICs. Non-Gaussianity is a commonly used measure for statistical independency. It can be given by the negentropy [17]

$$J(\mathbf{u}) = H(\mathbf{u}_{\text{Gauss}}) - H(\mathbf{u}) \tag{3}$$

where $\mathbf{u}_{\text{Gauss}}$ is a Gaussian random vector of the same covariance matrix as $\mathbf{u}$. $H(\cdot)$ is the entropy of a random vector $\mathbf{u}$. The negentropy is always non-negative and is zero if and only if the random variable has a Gaussian distribution. It is well justified as an estimator of the non-Gaussianity of the ICs. Since the exact probability density of the random variable is unknown, the exact negentropy computation using (3) above is prohibited. An approximation of the negentropy is proposed as follows:

$$J(u) \approx \{E[G(u)] - E[G(v)]\}^2 \tag{4}$$

where v is a Gaussian variable of zero mean and unit variance. $G(\cdot)$ is a non-quadratic function, which can be given by $G(u) = -\exp[-u^2/2]$, as suggested by Hyvarinen *et al.* [17]. The demixing matrix $\mathbf{W}$ with $\mathbf{U} = \mathbf{WX}$ that maximizes the negentropy can be efficiently calculated with the fixed-point search algorithm [26], [27] in FastICA.

To find a set of representative basis images, a collection of partitioned solar cells randomly chosen from the defect-free

solar modules are used as the input data set $\mathbf{X}$ in the off-line learning process. In the ICA model, each training sample of a 2D solar cell subimage must be reshaped as a 1D row vector in the data matrix $\mathbf{X}$. Denote by $f(r, c)$ the gray level at pixel coordinates (r, c) of an $M \times N$ subimage. The data matrix consists of B defect-free samples, i.e., $\mathbf{X} = [\mathbf{x}_1, \mathbf{x}_2, \ldots, \mathbf{x}_B]^{\text{T}}$, where $\mathbf{x}_i$ is the i-th training sample, and $\mathbf{x}_i = (x_{i1}, x_{i2}, \ldots, x_{iK})$ with $K = M \cdot N$. The 1D elements of $\mathbf{x}_i$ are obtained from the 2D subimage $f(r, c)$, i.e.,

$$x_{i, r+(c-1)\cdot M} = f(r, c) \tag{5}$$

for $r = 1, 2, \ldots, M$ and $c = 1, 2, \ldots, N$. The ICA model for the training data matrix $\mathbf{X}$ is given by

$$\mathbf{U} = \mathbf{W} \cdot \mathbf{X}.$$

The demixing matrix $\mathbf{W}$ is obtained from the FastICA algorithm [30]. The row vectors of the estimated sources with $\mathbf{U} = [\mathbf{u}_1, \mathbf{u}_2, \ldots, \mathbf{u}_B]^{\text{T}}$ are the basis images. Given a data set of B training subimages, we can obtain up to B basis images. They are used to extract discriminant features or reconstruct the image by representing the test image as a linear combination of the learned basis images $\mathbf{U}$.

C. On-Line Defect Inspection

For a solar module image under inspection, it is first divided into individual solar cell subimages by horizontal and vertical projections. The morphological operation then follows for each solar cell subimage to smooth the background. Let $\mathbf{y}$ be a solar cell subimage in its 1D form for test. The surface characteristics of this solar cell $\mathbf{y}$ can be represented by the coefficients of the linear combination of the basis images $\mathbf{U} = [\mathbf{u}_1, \mathbf{u}_2, \ldots, \mathbf{u}_B]$. That is

$$\mathbf{y} \approx \mathbf{b} \cdot \mathbf{U} = \sum_{i=1}^{B} b_i \cdot \mathbf{u}_i \tag{6}$$

where $\mathbf{b} = (b_1, b_2, \ldots, b_B)$ is the coefficient vector of the linear combination. It can be used as the feature vector of the test sample $\mathbf{y}$. The coefficient vector $\mathbf{b}$ can be obtained by

$$\mathbf{b} = \mathbf{y} \cdot \mathbf{U}^{+} \tag{7}$$

where $\mathbf{U}^{+}$ is the pseudo-inverse of $\mathbf{U}$, and is given by $\mathbf{U}^{\text{T}}(\mathbf{U} \cdot \mathbf{U}^{\text{T}})^{-1}$.

To determine the presence or absence of defects in the test sample $\mathbf{y}$, the cosine distance is used to evaluate the similarity between the test subimage $\mathbf{y}$ with feature vector $\mathbf{b}$ and every sample $\mathbf{x}_i$ with feature vector $\mathbf{b}_i$ in the training data set $\mathbf{X}$. Hence, the cosine distance $\Delta d(\mathbf{y}, \mathbf{x}_i)$ is defined as

$$\Delta d(\mathbf{y}, \mathbf{x}_i) = 1 - \cos(\mathbf{y}, \mathbf{x}_i) = 1 - \frac{\mathbf{b} \cdot \mathbf{b}_i}{\|\mathbf{b}\| \cdot \|\mathbf{b}_i\|} \tag{8}$$

where the feature vector $\mathbf{b}_i$ of training sample $\mathbf{x}_i$ is given by

$$\mathbf{b}_i = \mathbf{x}_i \cdot \mathbf{U}^{+}. \tag{9}$$

A cosine distance of zero is obtained if the two compared subimages are identical. The final cosine distance of the test sample $\mathbf{y}$ is given by the one with the minimum value among all the training samples in the data set $\mathbf{X}$, i.e.,

$$\Delta d(\mathbf{y}) = \min_{\mathbf{x}_i \in \mathbf{X}} \{\Delta d(\mathbf{y}, \mathbf{x}_i)\}. \tag{10}$$

If the minimum cosine distance $\Delta d(\mathbf{y})$ is larger than some predetermined threshold, the test sample $\mathbf{y}$ is classified as a defective one. Otherwise, it is claimed to be defect-free.

Since the feature extraction approach is based on the distance measure of the test sample with respect to every training sample in the data set, the choice of defect-free solar cell subimages used in the training data set becomes very critical. We therefore also propose a self-referential image reconstruction process to detect the presence/absence of defects in a test image. Any test sample $\mathbf{y}$ can be reconstructed from the basis images $\mathbf{U}$ by

$$\hat{\mathbf{y}} = \mathbf{b} \cdot \mathbf{U} \tag{11}$$

where $\mathbf{b}$ is the coefficient vector as defined in (7). The reconstruction error of the test sample $\mathbf{y}$ is defined as

$$\Delta \varepsilon(\mathbf{y}) = \|\mathbf{y} - c \cdot \hat{\mathbf{y}}\| \tag{12}$$

where the constant c is used as a regularization, and is given by

$$c = \frac{\|\mathbf{y}\|}{\|\hat{\mathbf{y}}\|}. \tag{13}$$

If the test sample contains defects, we expect that it cannot be well reconstructed from the defect-free basis images and the resulting reconstruction error should be distinctly large. If the reconstruction error is larger than some pre-determined threshold, the test sample $\mathbf{y}$ is identified as a defective one. Otherwise, it is classified as a defect-free solar cell subimage.

For self-referential image reconstruction with ICA, there is a special finding that is worth noting here. Because the demixing matrix $\mathbf{W}$ given by the FastICA algorithm is orthogonalized, it indicates that $\mathbf{W}^{\mathrm{T}} \cdot \mathbf{W} = \mathbf{I}$. The reconstruction of a test sample $\mathbf{y}$ can be thus given by

$$\begin{aligned}
\hat{\mathbf{y}} = \mathbf{b} \cdot \mathbf{U} &= \mathbf{b}(\mathbf{W}\mathbf{X}) = (\mathbf{y} \cdot \mathbf{U}^+)(\mathbf{W}\mathbf{X}) \\
&= \mathbf{y}(\mathbf{W}\mathbf{X})^{\mathrm{T}}[(\mathbf{W}\mathbf{X}) \cdot (\mathbf{W}\mathbf{X})^{\mathrm{T}}]^{-1}(\mathbf{W}\mathbf{X}) \\
&= \mathbf{y} \cdot \mathbf{X}^{\mathrm{T}}[\mathbf{X} \cdot \mathbf{X}^{\mathrm{T}}]^{-1} \cdot \mathbf{X} \\
&= (\mathbf{y} \cdot \mathbf{X}^+) \cdot \mathbf{X}.
\end{aligned} \tag{14}$$

In the equation above, $\mathbf{y} \cdot \mathbf{X}^+$ is the coefficient vector for the linear combination of the original data matrix $\mathbf{X}$. Therefore, the image reconstruction approach for detecting the presence/absence of defects in a test sample $\mathbf{y}$ does not require the ICA optimization search, i.e., the learning stage can be omitted. The original data set $\mathbf{X}$ itself forms the basis images and the same reconstruction error can be obtained either from the ICA basis images $\mathbf{U}$ or from the original training images $\mathbf{X}$.

The proposed method needs to calculate the coefficient vector $\mathbf{b}$ using (7) and then reconstruct the inspection image $\mathbf{y}$ from the basis images $\mathbf{U}$ using (11). Given an image of size $M \times N$ and B basis images, the reshaped 1-D image $\mathbf{y}$ is of size $1 \times K$ with $K = M \cdot N$ and the matrix $\mathbf{U}$ is of size $B \times K$, the

computational complexity is $K(K \cdot B)$ for the coefficient vector $\mathbf{b}$ and $B(B \cdot K)$ for the reconstruction image $\hat{\mathbf{y}}$. Therefore, the overall computational complexity is $K^2 \cdot B + B^2 \cdot K$. The computation can be easily and efficiently executed with matrix operations.

III. EXPERIMENTAL RESULTS

This section presents the experimental results from a number of multicrystalline solar modules in EL images to evaluate the performance of the proposed method. All proposed algorithms and experiments were implemented on a personal computer with a Pentium Core 2 Duo 3.00 GHz processor. The whole image of a solar module is 1250×1250 pixels wide with 8-bit gray levels. The solar module under test comprises a matrix of 36 solar cells, each of image size 208×208 pixels. The proposed ICA-based defect detection method is highly dependent on the defect-free training samples for extracting representative basis images. Especially, the image reconstruction approach evaluates the reconstruction error directly from the original training samples. Different defect-free samples used to generate the representative basis images may produce different detection results. Therefore, we conducted 10 training sets of randomly chosen defect-free samples for the experiments. Each training set contains 30 random defect-free solar cell subimages and, thus, each data set creates a different combination of 30 basis images.

The performance of the proposed method under different scenarios (e.g., input images with and without morphological smoothing, and feature extraction approach vs. image-reconstruction approach) is evaluated by the recognition rate. It is defined as

$$\mathrm{R}\% = \frac{N_T - (N_{FN} + N_{FP})}{N_T} \cdot 100\%$$

where N_T is the total number of test samples;

N_{FN} is the number of mis-detected defect samples;

N_{FP} is the number of falsely-detected defect-free samples.

In order to identify defective solar cells with large reconstruction errors $\Delta \varepsilon$, we use the simple statistical control limit to set the threshold value. It is given by

$$\mu_{\Delta \varepsilon} + C \cdot \sigma_{\Delta \varepsilon}$$

where $\mu_{\Delta \varepsilon}$ and $\sigma_{\Delta \varepsilon}$ are the mean and standard deviation of $\Delta \varepsilon$ from a set of defect-free test samples. The parameter C is a control constant. It is given by 3 in this study to follow the commonly-used 3-sigma rule in statistical process control. Likewise, the threshold for cosine distance $\Delta d(\mathbf{y})$ is also determined by the statistical control limit. In the experiments, there are a total of 80 solar cell subimages used as the test samples, of which 28 are defect-free and 52 are defective. The test samples used in the experiments were provided by a local solar cell manufacturer. The quality engineers care more about the detection capability for various defect types that may present randomly in any locations in solar modules.

TABLE I
RECOGNITION RATES OF ICA-BASED FEATURE EXTRACTION AND IMAGE
RECONSTRUCTION APPROACHES

| Training data set | Detection method | |
	Feature extraction Δd	Image reconstruction $\Delta \varepsilon$
1	81.3%	92.5%
2	73.8%	92.5%
3	82.5%	97.5%
4	78.8%	87.5%
5	82.5%	92.5%
6	80.0%	93.7%
7	73.8%	92.5%
8	82.5%	95.0%
9	75.0%	98.7%
10	73.8%	91.2%
Mean	78.4%	93.4%
Std. dev.	3.9%	3.2%

Fig. 6. Receiver operating characteristic (ROC) curves of the ICA-based feature extraction and image reconstruction approaches.

The first experiment was conducted to evaluate the performance between the feature-extraction $\Delta d(\mathbf{y})$ and the image-reconstruction $\Delta \varepsilon(\mathbf{y})$. The morphological preprocessing is applied to both ICA approaches, and the number of basis images is 30. Table I summarizes the statistics of recognition rates R% of the two ICA methods for the 10 training data sets. It shows that the average recognition rate of the image reconstruction approach is 93.4% with a maximum of 98.7%, while the average recognition rate of the feature extraction approach is only 78.4% with a maximum of 82.5%. The "Std. dev." in the table means the standard deviation of recognition rate $R\%$ obtained from the 10 training sets. Table I shows that most of the 10 training sets can yield a good recognition rate larger than 92% and the standard deviation is only 3.2% for the image reconstruction approach. The variation is due to the different basis images derived from individual training samples. If the training samples contain good representations of various background patterns of defect-free solar cells, the derived basis images can then sufficiently represent all possible background patterns of the test samples. Since the training process can be performed off-line, we can always carry out multiple training sets that contain different defect-free samples in a preliminary experiment and then select the one that results in the maximum recognition rate for on-line inspection in manufacturing.

To further compare the performance of these two approaches, the receiver operating characteristic (ROC) curves are also given in Fig. 6 for the 9th training data set that gives the best recognition rate. In the ROC plot, the true positive (TP) rate is shown in the vertical axis and the false positive (FP) rate is shown in the horizontal axis. The results show that the ROC curve of the image reconstruction approach rises swiftly upward and far outperforms the feature extraction approach. The image reconstruction method uses the whole image ($M \cdot N$ data points of an $M \times N$ image) to calculate the reconstruction error. It performs the self-comparison between the input image and the template image pixel by pixel, where the template image is generated from the input image itself. However, the feature-extraction method uses only a small number of B data points, where B is the number of basis images, to calculate the difference of feature vectors between the inspection image and each individual defect-free image used in the training set.
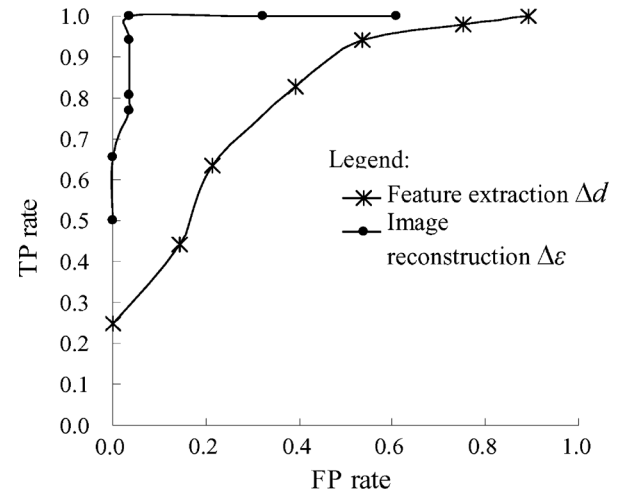
Therefore, the feature-extraction method may result in severe deviation when the inspection image is quite different from any of the training samples. Since the image reconstruction method uses more data points and evaluates the errors from the image itself, it is more stable and reliable to generate a good discrimination measurement to detect the presence/absence of defects in a solar cell subimage. In the subsequent experiments, only the image reconstruction approach under different scenarios is evaluated accordingly.

The second experiment was conducted to evaluate the performance of the proposed image reconstruction approach with and without morphological smoothing. The number of basis images used in the experiment is also 30. Table II lists the recognition rates with the original EL images as the input and those with the morphologically-smoothed images as the input. It shows that the morphological smoothing process can slightly improve the mean recognition rate by 2%. For all 10 training data sets, the recognition rates of morphologically-smoothed images are consistently larger than those of original EL images. The morphological process tends to smooth (or remove) the dark regions in the background and generate a more simple and uniform surface so that the basis images can have a better representation for arbitrary EL images. The dark regions in the background are very difficult to be smoothed while the defective regions are clearly retained at the same time. The proposed morphological process can mildly smooth or blur the dark regions in the background and, thus, the resulting EL images can be better represented from a given set of basis images. This gives a slight improvement on recognition rate. The experimental results indicate that the proposed image reconstruction method can further improve the recognition rate if a more effective background smoothing process can be developed in the future.

The last experiment in this paper is to evaluate the effect of changes in the number of training images (i.e., the number of basis images). The proposed image reconstruction approach with morphological smoothing is applied in the experiment. Table III summarizes the statistics of recognition rates with varying number of basis images from 20, 25, 30 to 40. It shows that the recognition rate increases as the number of basis images

Training data set	Input images	
	Original EL images	Morphologically-smoothed images
1	91.2%	92.5%
2	91.2%	92.5%
3	95.0%	97.5%
4	87.5%	87.5%
5	91.2%	92.5%
6	90.0%	93.7%
7	91.2%	92.5%
8	91.2%	95.0%
9	95.0%	98.7%
10	91.2%	91.2%
Mean	91.5%	93.4%
Std. dev.	2.2%	3.2%

TABLE III
EFFECT OF THE NUMBER OF BASIS IMAGES ON THE RECOGNITION RATE

Training data set	Number of basis images			
	20	25	30	40
1	91.2%	90.0%	92.5%	92.5%
2	91.2%	92.5%	92.5%	92.5%
3	96.5%	97.5%	97.5%	97.5%
4	91.2%	88.7%	87.5%	87.5%
5	92.5%	92.5%	92.5%	92.5%
6	86.5%	91.2%	93.7%	93.7%
7	90.0%	90.0%	92.5%	92.5%
8	95.0%	95.0%	95.0%	95.0%
9	97.5%	98.7%	98.7%	98.7%
10	86.2%	91.2%	91.2%	91.2%
Mean	91.8%	92.7%	93.4%	93.4%
Std. dev.	3.8%	3.3%	3.2%	3.2%

is added up to 30. A small number of basis images of 20 also generate a good mean recognition of 91.8%. A larger number of basis images of 40 cannot further improve the recognition rate. In this study, each individual inspection image is reconstructed from a linear combination of a given set of basis images. If the derived basis images cannot sufficiently represent a variety of crystal-grain backgrounds in EL images, the resulting reconstruction errors could be very large even for defect-free test images. With less training samples, the limited number of basis images cannot well represent all possible defect-free background patterns. Both defect-free and defective EL images may thus generate large reconstruction errors in a similar range, and the resulting measurement cannot distinctly discriminate the defective images from the normal ones. When the number of training examples is sufficiently large, more training examples give only redundant representations of crystal-grain background patterns in EL images and cannot further improve the recognition rate.

Most of the currently available algorithms for solar wafer/cell inspection such as [11], [16] are either based on adaptive thresholding followed by binary morphology and blob analysis or based on gray-level morphology followed by region-segmentation and blob analysis. We therefore compare the proposed method with such thresholding/morphology approaches. The four solar cell samples demonstrated in Fig. 5 are used for the performance comparison. Fig. 7(a1)–(d1) shows repeatedly the four test samples. Fig. 7(a2)–(d2) presents the detection results

from the adaptive thresholding, followed by a 11×11 binary morphological closing and blob analysis for elongated objects, where black objects are final detected faulty items and the gray objects are the intermediate results of binary morphology. The experiment shows that the finger interruptions can be detected. It fails to identify the subtle micro-cracks, and presents severe noise. Threshlding-based methods require a higher defect contrast than the grain boundary contrast in the EL image. However, the defective image shown in Fig. 7(d1) contains a small crack with gray values larger than those of grain edges. The thresholding method thus mis-detects the crack and presents some grain edge points as noise in the segmented image. Fig. 7(a3)–(d3) further shows the detection results of gray-level morphology. The original solar cell subimage is first smoothed by gray-level morphological closing with 5×13 structuring elements at $0°$, $45°$, $90°$ and $135°$ directions to remove the possible defects. The original image is then subtracted from the smoothed image. Blob analysis for elongated objects is finally carried out to identify the defective regions. The experiment shows that it can detect some of the finger interruptions and the small micro-crack with severe noise. In the EL image, the crystal grains could be cloud-shaped and very large in size in the background. There are no effective morphological operations that can remove thin elongated defects and preserve cloud-shaped grains at the same time, or vice versa. Severe false alarms for defect-free solar cells are thus generated. The proposed method can identify correctly all these four test samples. The comparative methods of adaptive thresholding and gray-level morphology are also applied to the 80 test samples aforementioned in this section. The two comparative methods perform poorly with recognition rates lower than 50%, which are worse than random guess.

IV. CONCLUSION

In this paper, we have proposed defect detection methods based on ICA basis images to detect defective solar cell subimages of a large solar module in the electroluminescence image. The line- and bar-shaped defects of micro-cracks, breaks and finger interruptions in the solar module can be well presented as dark regions in the EL image. However, the EL image also displays the dislocations and grain boundaries of the multicrystalline solar wafer as dark regions and results in a random inhomogeneous background. The dark regions of defects and those in the defect-free background can be visually observed in the EL image, but they are extremely difficult to be distinguished automatically.

We have evaluated two discrimination approaches based on ICA basis images. The first feature extraction approach represents the test image under inspection as a linear combination of the basis images and takes the coefficients as the feature vector. The minimum cosine distance of feature vectors between the test image and all training samples is then used as the discrimination measure. The second image reconstruction approach synthesizes the test image by the linear combination of the basis images. The reconstruction error between the test image and its reconstructed image is then used as the discrimination measure. Experimental results show that the image reconstruction approach distinctly outperforms the feature extraction approach
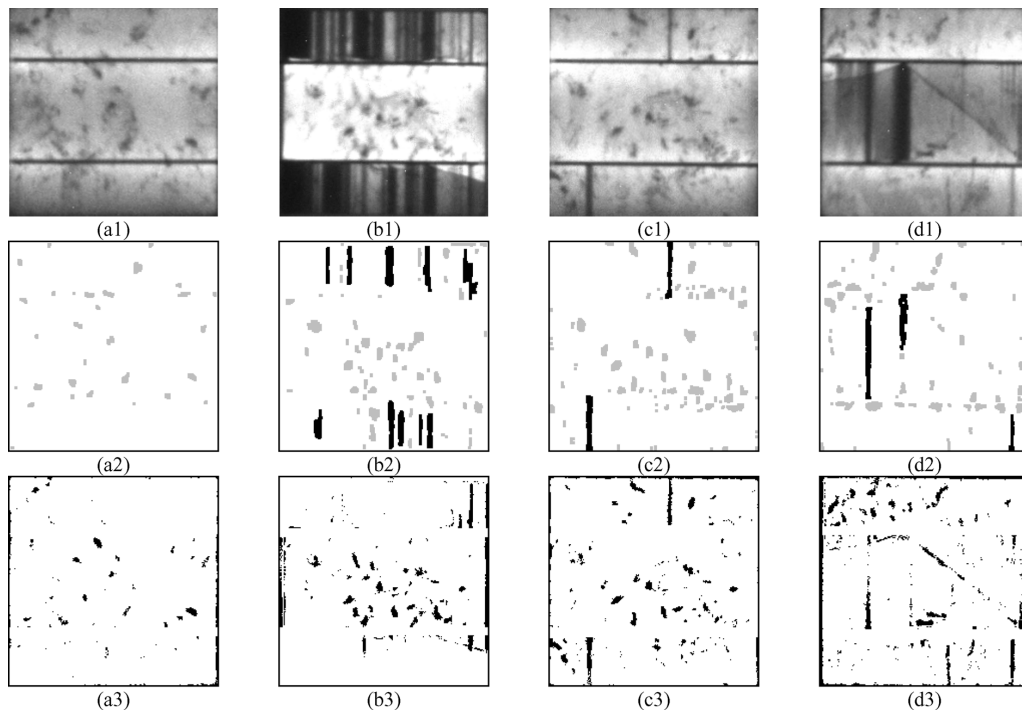
Fig. 7.   Comparison of the proposed method with adaptive thresholding/morphology approaches: (a1)–(d1) EL images of one defect-free and 3 defective solar cells for testing; (a2)–(d2) respective detection results from adaptive thresholding and binary morphology; (a3)–(d3) respective detection results from gray-level morphology.

and it can use the original defect-free training samples as the basis images without the need of ICA process for learning. The overall recognition rate of the image reconstruction approach is 93.4% for the inspection of solar cell subimages. The computation time of image reconstruction and measurement of reconstruction error is only 0.03 seconds with 30 basis images for a 208×208 solar cell subimage, or 1.08 seconds for a whole solar module image containing 36 solar cells. It is computationally very efficient for a large solar module of image size 1250×1250 pixels.

The additional processing time of the morphological operation is 0.04 seconds for a 208×208 solar cell subimage or 1.44 seconds for a whole solar module image of 1250×1250. A more efficient smoothing preprocessing that can effectively remove the random dark regions in the background for better basis image extraction and representation is worth further investigation.

The proposed method in this study can be treated as a "global" approach that detects only the presence/absence of defects in solar modules. It cannot classify the type of defect. A "local" approach that detects the shape and location of a defect in the EL image using a more complicated spectral technique such as the Fourier transform or the wavelet transform is currently under investigation. The "local" approach generally could be computationally more intensive. Since a solar module involves a very large image size, the "global" approach can efficiently screen the suspected defective solar cells and then the "local" approach can effectively verify and detect the actual shape and location of a defect for the suspected solar cells. The incorporation of both "global" and "local" approaches can then both efficiently and effectively identify defects of solar modules in EL images.

REFERENCES

[1] Y. Si, J. Mei, and H. Gao, "Novel approaches to improve robustness, accuracy and rapidity of iris recognition systems," *IEEE Trans. Ind. Inf.*, vol. 8, pp. 110–117, Feb. 2012.

[2] S. Jin, D. Kim, T. T. Nguyen, D. Kim, M. Kim, and J. W. Jeon, "Design and implementation of a pipelined datapath for high-speed face detection using FPGA," *IEEE Trans. Ind. Inf.*, vol. 8, pp. 158–167, Feb. 2012.

[3] R. Gerndt, S. Michalik, and S. Krupop, "Embedded vision system for robotics and industrial automation," in *IEEE Int. Conf. Ind. Inf. (INDIN)*, Caparica, Lisbon, 2011, pp. 895–899.

[4] S. Livatino, F. Banno, and G. Muscato, "3-D integration of robot vision and laser data with semiautomatic calibration in augmented reality stereoscopic visual interface," *IEEE Trans. Ind. Inf.*, vol. 8, pp. 69–77, Feb. 2012.

[5] C.-H. Chan and G. K. H. Pang, "Fabric defect detection by Fourier analysis," *IEEE Trans. Ind. Appl.*, vol. 36, pp. 1267–1276, 2000.

[6] A. Picon, O. Ghita, P. F. Whelan, and P. M. Iriondo, "Fuzzy spectral and spatial feature integration for classification of nonferrous materials in hyperspectral data," *IEEE Trans. Ind. Inf.*, vol. 5, pp. 483–494, 2009.

[7] D.-M. Tsai, I.-Y. Chiang, and Y.-H. Tsai, "A shift-tolerant dissimilarity measure for surface defect detection," *IEEE Trans. Ind. Inf.*, vol. 8, pp. 128–137, Feb. 2012.

[8] T. Fuyuki and A. Kitiyanan, "Photographic diagnosis of crystalline silicon solar cells utilizing electroluminescence," *Appl. Phys. A*, vol. 96, pp. 189–196, July 2009.

[9] T. Fuyuki, H. Kondo, T. Yamazaki, Y. Takahashi, and Y. Uraoka, "Photographic surveying of minority carrier diffusion length in polycrystalline silicon solar cells by electroluminescence," *Appl. Phys. Lett.*, vol. 86, p. 262108, Jun. 2005.

[10] Y. Takahashi, Y. Kaji, A. Ogane, Y. Uraoka, and T. Fuyuki, "Luminoscopy—Novel tool for the diagnosis of crystalline silicon solar cells and modules utilizing electroluminescence," in *Proc. 4th World Conf. Photovoltaic Energy Conv.*, Hawaii, 2006, pp. 924–927.

[11] Z. Fu, Y. Zhao, Y. Liu, Q. Cao, M. Chen, J. Zhang, and J. Lee, "Solar cell crack inspection by image processing," in *Proc. Int. Conf. Business Electronic Product Reliability Liability*, Shanghai, China, 2004, pp. 77–80.

[12] M. A. Ordaz and G. B. Lush, "Machine vision for solar cell characterization," in *Proc. SPIE*, San Jose, CA, 2000, pp. 238–248.

[13] M. Pilla, F. Galmiche, and X. Maldague, "Thermographic inspection of cracked solar cells," in *Proc. SPIE*, Orlando, FL, USA, 2002, pp. 699–703.

[14] D. M. Tsai, C. C. Chang, and S. M. Chao, "Micro-crack inspection in heterogeneously textured solar wafers using anisotropic diffusion," *Image Vis. Comput.*, vol. 28, pp. 491–501, Mar. 2010.

[15] D. M. Tsai and J. Y. Luo, "Mean shift-based defect detection in multicrystalline solar wafer surfaces," *IEEE Trans. Ind. Inf.*, vol. 7, pp. 125–135, Feb. 2011.

[16] Y. C. Chiou, F. Z. Liu, and Y.-T. Liang, "Micro crack detection of multi-crystalline silicon solar wafer using machine vision techniques," *Sensor Rev.*, vol. 31, pp. 154–165, 2011.

[17] A. Hyvarinen, J. Karhunen, and E. Oja, *Independent Component Analysis*. New York: Wiley, 2001.

[18] R. Manduchi and J. Portilla, "Independent component analysis of textures," in *Proc. IEEE Int. Conf. Comput. Vis.*, Kerkyra, Greece, 1999, pp. 1054–1060.

[19] R. Jenssen and T. Eltoft, "Independent component analysis for texture segmentation," *Pattern Recognit.*, vol. 36, pp. 2301–2315, Oct. 2003.

[20] S. Serdaroglu, A. Ertuzun, and A. Ercil, "Defect detection in textile fabric images using wavelet transforms and independent component analysis," *Pattern Recognit. Image Anal.*, vol. 16, pp. 61–64, Jan. 2006.

[21] O. G. Sezer, A. Ercil, and A. Ertuzun, "Using perceptual relation of regularity and anisotropy in the texture with independent component model for defect detection," *Pattern Recognit.*, vol. 40, pp. 121–133, Jan. 2007.

[22] C. J. Lu and D. M. Tsai, "Independent component analysis-based defect detection in patterned liquid crystal display surfaces," *Image Vis. Comput.*, vol. 26, pp. 955–970, Jul. 2008.

[23] G. Polder and G. W. A. M. van der Heijden, "Tomato sorting using independent component analysis on spectral images," *Real-Time Imaging*, vol. 9, pp. 253–259, Aug. 2003.

[24] A. Hyvarinen and E. Oja, "Independent component analysis: Algorithms and applications," *Neural Networks*, vol. 13, pp. 411–430, Jun. 2000.

[25] A. J. Bell and T. J. Sejnowski, "An information-maximization approach to blind separation and blind deconvolution," *Neural Comput.*, vol. 7, pp. 1129–1159, Nov. 1995.

[26] A. Hyvarinen and E. Oja, "A fast fixed-point algorithm for independent component analysis," *Neural Comput.*, vol. 9, pp. 1483–1492, Oct. 1997.

[27] A. Hyvarinen, "Fast and robust fixed-point algorithms for independent component analysis," *IEEE Trans. Neural Netw.*, vol. 10, pp. 626–634, May 1999.

[28] R. Boscolo, H. Pang, and V. P. Roychowdhury, "Independent component analysis based on nonparametric density estimation," *IEEE Trans. Neural Netw.*, vol. 15, pp. 55–65, Jan. 2004.

[29] T. Blaschke and L. Wiskott, "CuBICA: Independent component analysis by simultaneous third- and fourth-order cumulant diagonalization," *IEEE Trans. Signal Process.*, vol. 52, pp. 1250–1256, May 2004.

[30] J. Hurri, H. Gavert, J. Sarela, and A. Hyvarinen, FastICA Package [Online]. Available: http://www.cis.hut.fi/projects/ica/fastica/

Du-Ming Tsai received the B.S. degree in industrial engineering from the Tunghai University, Taiwan, in 1981, and the M.S. and Ph.D. degrees in industrial engineering from Iowa State University, Ames, in 1984 and 1987, respectively.

From 1988 to 1990, he was a Principal Engineer of Digital Equipment Corporation, Taiwan, where his work focused on process and automation research and development. Currently he is a Professor of Industrial Engineering and Management at the Yuan-Ze University, Taiwan. His research interests include automated visual inspection, object recognition and texture analysis.

Wei-Yao Chiu received the B.S. degree in industrial management from the Chung-Hua University, Taiwan, in 2005 and the M.S. degrees in industrial engineering and management from the Yuan-Ze University, Taiwan, in 2007, where he is currently pursuing the Ph.D. degree in industrial engineering and management.

His research interests include automated visual inspection and video surveillance.